Int. J. Solids Structures, 1973, Vol. 9, pp. 31 to 52. Pergamon Press. Printed in Great Britain

CUSPED WAVE FRONTS IN ANISOTROPIC ELASTIC PLATES

P. W. RANDLES†

Assistant Professor of Mechanical Engineering, University of Wyoming, Laramie, Wyoming 82070

Abstract—A method, applied previously to isotropic plates, is extended to anisotropic plates to obtain the high-frequency transient response for cases where some of the wave fronts are cusped. A multitude of wave fronts are found, which result from the multiple reflections in the plate and which are not present in the isotropic case or in some anisotropic cases. Wave-front approximations and the approximate response near the tips of cusped wave fronts are derived from integral representations for the response.

1. INTRODUCTION

THE method given by the author and Miklowitz [1] for obtaining convenient high-frequency modal representations for the response of an infinite, homogeneous, isotropic, linearly elastic plate is extended to certain anisotropic plate materials. The emphasis is on materials for which cusped wave fronts are expected about the loaded face of the plate; other cases being very similar to the isotropic case. An impulsive normal line load is considered, although the method applies for any impulsive loading which initiates plane strain motions and for which a modal solution can be obtained. The lowest modes, which contain the surface waves and the low-frequency compressional and flexural waves, are not included in this work.

There is a moderately long history of work on wave propagation problems in anisotropic elastic solids. Even so, only in recent years have transient solutions appeared for geometries more complicated than the infinite space. Musgrave [2] first realized that cusps could occur on some of the wave fronts if the elastic constants satisfy certain conditions. The presence of these cusps greatly complicates the mathematics. Kraut [3] overcame these difficulties for a half-space problem by using Cagniard's method in conjunction with considerable analysis of difficult integrals in the complex plane. Scott and Miklowitz [4] used Cagniard's method to obtain wave-front expansions for the more complicated plate geometry, but for cases where cusps were not present.

The purpose here is to by-pass Cagniard's method, which has not been used for plate problems involving cusped wave fronts and use a method resulting in accurate high-frequency representations. This approach is not complicated by the presence of some cusped wave fronts, as contrasted with Cagniard's method, and is only slightly complicated by cusped wave fronts about the loaded plate face.

This method takes the modal solution as a starting point and ultimately results in a solution in which individual terms in an integral representation can be identified with the response associated with individual wave fronts in the plate. The resulting representation can be evaluated numerically or approximated to obtain very accurate high-frequency representations for the response of the plate. This solution is more substantial than single-term wave-front expansions obtained by ray techniques, and it is independent of the corresponding half-space solution.

† Now at McDonnell Douglas Astronautics Company, Huntington Beach, California 92647.

The modal solution is written in new variables in Section 2, which requires considerable knowledge of the branches of the frequency equation. An altered form of the modal solution is given in Section 3, which is amenable to high-frequency approximations and which readily exhibits the response associated with individual wave fronts. The solution is approximated in Section 4 and the wave-front geometry is discussed in Section 5. Various interesting wave fronts come to light as a result of the multiple reflections in the plate and the presence of cusps. The solution is further approximated in Section 6 to obtain information near singular wave fronts, including the region near cusp tips. The approximate response at a specific time and location in the plate is obtained.

2. THE MODAL SOLUTION IN THE χ, η VARIABLES

A class of anisotropic plate materials is considered for which all of the elastic constants c_{ij} (notation used by Love [5]) are zero except for $i, j = 1$–3 and $i = j = 4$–6. With $c_{ij} = c_{ji}$, nine independent elastic constants, at most, remain. The same class of materials was treated by Scott and Miklowitz [4]. An isotropic material certainly belongs to this class, along with orthorhombic, tetragonal, cubic and hexagonal crystals, and orthotropic and transversely isotropic materials. Positive definiteness of the strain energy function requires that c_{11}, $c_{33}, c_{55} > 0$ and that $c_{11}c_{33} > c_{13}^2$. Further, it is assumed that $c_{11}, c_{33} > c_{55}$, as is the case in most real materials.

Plane strain motions ($\varepsilon_{22} = 0$) are possible in this class of anisotropic materials and only two of the three basic waves are coupled through reflections at a free boundary $x_3 = \text{const}$. There are only two thickness wave numbers associated with these coupled waves. Further, if the x_2 displacement component is zero and all other quantities are independent of x_2, then the stress component $\sigma_{23} \equiv 0$.

The plane strain equations of motion of linear elasticity for these anisotropic materials are

$$\frac{\partial \sigma_{11}}{\partial x_1} + \frac{\partial \sigma_{13}}{\partial x_3} = \rho \frac{\partial^2 u}{\partial t^2}, \qquad \frac{\partial \sigma_{13}}{\partial x_1} + \frac{\partial \sigma_{33}}{\partial x_3} = \rho \frac{\partial^2 w}{\partial t^2} \tag{1}$$

where

$$\sigma_{11} = c_{11}\frac{\partial u}{\partial x_1} + c_{13}\frac{\partial w}{\partial x_3}, \qquad \sigma_{13} = c_{55}\left(\frac{\partial u}{\partial x_3} + \frac{\partial w}{\partial x_1}\right), \qquad \sigma_{33} = c_{13}\frac{\partial u}{\partial x_1} + c_{33}\frac{\partial w}{\partial x_3}.$$

The displacement components in the x_1- and x_3-directions are u and w, respectively.

The infinite plate $-H \leq x_3 \leq H$ is subjected to the boundary conditions (δ and δ_+ are delta functions)

$$\sigma_{33}(x_1, H, t) = -I_0\delta(x_1)\delta_+(t), \qquad \sigma_{33}(x_1, -H, t) = 0, \qquad \sigma_{13}(x_1, \pm H, t) = 0, \tag{2}$$

and is quiescent for $t \leq 0$. The radiation condition requires that all dependent variables vanish as $|x_1| \to \infty$. The constant I_0 is the impulse per unit length along the line of loading.

The formal solution of this problem results by employing a Laplace transform on t and a Fourier transform on x_1. The modal solution remains after the Laplace inversion as an infinite sum of residues from the zeros of the frequency equation. Such solutions are found in the work of Scott and Miklowitz [4, 6] and the derivation is not repeated here. However, some discussion of the modal solution is given.

Mathematically, the most difficulty in evaluating the modal solution occurs if

$$(c_{13}+c_{55})^2 > c_{33}(c_{11}-c_{55}), \tag{3}$$

which, according to Musgrave [2], is the condition for cusped wave fronts about the plate face $x_3 = H$. It will be assumed throughout that (3) holds and the simpler cases where (3) is violated will be discussed only in passing.

The two thickness wave numbers occurring in this solution are α_j, $j = 1, 2$, given by

$$\begin{aligned} 2c_{33}c_{55}\alpha_j^2 = {} & (c_{33}+c_{55})\rho\omega^2 - [c_{11}c_{33}+c_{55}^2-(c_{13}+c_{55})^2]\kappa^2 + (-1)^j\{[(c_{11}^{\frac{1}{2}}c_{33}^{\frac{1}{2}}-c_{55})^2 \\ & -(c_{13}+c_{55})^2][(c_{11}^{\frac{1}{2}}c_{33}^{\frac{1}{2}}+c_{55})^2-(c_{13}+c_{55})^2]\kappa^4 \\ & -2[(c_{33}-c_{55})(c_{11}c_{33}-c_{55}^2)-(c_{33}+c_{55})(c_{13}+c_{55})^2]\rho\kappa^2\omega^2 \\ & +(c_{33}-c_{55})^2\rho^2\omega^4\}^{\frac{1}{2}} \end{aligned} \tag{4}$$

where ω is the frequency and κ is the wave number, as well as being the integration variable in the modal solution. For definiteness, $\alpha_j = |\alpha_j|$ is taken when α_j is real and $\alpha_j = -i|\alpha_j|$ when it is pure imaginary.

The rather complicated frequency equation in the κ, ω variables, not listed here, has branches $\omega = \omega(\kappa)$, which are investigated and discussed in the literature, generally for κ and ω not large. Some of these references are Anderson [7], Abubakar [8] and Kaul and Mindlin [9], the last being for the more complicated monoclinic crystal plate.

The reasons for replacing the κ, ω variables are even more compelling than for the isotropic case [1]. The following solution depends at many stages on the new variables and, significantly, it is not much more difficult than the isotropic case in these variables. In the κ, ω variables, the problem verges on the impossible.

The new variables are

$$\chi = (\alpha_2-\alpha_1)/(\alpha_2+\alpha_1), \qquad \eta = H(\alpha_2+\alpha_1) \tag{5}$$

with χ replacing κ as the integration variable in the modal integrals.

The inverse functions are

$$\begin{aligned} \alpha_j &= \eta[1+(-1)^j\chi]/2H, \qquad j = 1, 2, \\ \kappa &= \eta[c_1(1+\chi^2)+c_2(g(\chi))^{\frac{1}{2}}]^{\frac{1}{2}}/2H, \\ \omega &= (c_{55}/\rho)^{\frac{1}{2}}\eta[c_3(1+\chi^2)+c_4(g(\chi))^{\frac{1}{2}}]^{\frac{1}{2}}/2H \end{aligned} \tag{6}$$

where

$$g(\chi) = (1+\chi^2)^2 - c_5(1-\chi^2)^2$$

and the constants c_j, $j = 1$–5, are listed in the Appendix. The branches of the outer radicals in (6) are chosen so that κ and ω are nonnegative when they are real for $\mathrm{Re}(\eta) \geq 0$. Re( ) and Im( ) denote real and imaginary parts of a complex quantity. The branches of $(g(\chi))^{\frac{1}{2}}$, both of which are involved, are defined in the following.

The branch points of $(g(\chi))^{\frac{1}{2}}$ are located at χ_{cr}, $-1/\chi_{cr}$, $-\chi_{cr}$ and $1/\chi_{cr}$ where

$$\chi_{cr} = \exp(i\theta_{cr}), \qquad \theta_{cr} = \tan^{-1}[(-c_5)^{-\frac{1}{2}}] \tag{7}$$

with $0 < \theta_{cr} < \pi/2$. The Riemann surface of $(g(\chi))^{\frac{1}{2}}$ is defined by taking branch cuts on $\chi = e^{i\theta}$ between χ_{cr} and $-1/\chi_{cr}$ ($\theta_{cr} \leq \theta \leq \pi-\theta_{cr}$) and between $1/\chi_{cr}$ and $-\chi_{cr}$ ($-\theta_{cr} \geq \theta \geq \theta_{cr}-\pi$). The branches of $(g(\chi))^{\frac{1}{2}}$ are defined by making $(g(\chi))^{\frac{1}{2}}$ positive on sheet (I) and

negative on sheet (II) for χ real. (I) and (II) will be used throughout to designate these sheets and quantities on them.

If (3) does not hold, these branch points are either on the Im(χ)- or Re(χ)-axis. For the isotropic case, $c_5 = 1$ and the branch points merge at $\chi = 0, \infty$ making $(g(\chi))^{\frac{1}{2}} = \pm 2\chi$.

The frequency equation in the variables (5) takes exactly the same form

$$\sin(\eta) \pm R(\chi) \sin(\chi\eta) = 0 \tag{8}$$

as in the isotropic case. The signs relate to symmetrical (+) and asymmetrical (−) waves with respect to the midplane $x_3 = 0$ of the plate. The simple form of (8) is fortunate since a detailed investigation of the branches $\eta(\chi)$ is contained in [10]. The only complication is the function $R(\chi)$. While $R(\chi)$ is a rational function of χ and Poisson's ratio for the isotropic case, it now takes the form

$$R(\chi) = R(\chi, c_{11}, c_{33}, c_{13}, c_{55}) = [r(\chi)+r(-\chi)]/[r(\chi)-r(-\chi)] \tag{9}$$

where

$$r(\chi) = (1-\chi)[(1+\chi)^2 + c_6(1+\chi^2) - c_6(g(\chi))^{\frac{1}{2}}][-(1-\chi)^2 + c_7(1+\chi^2) + c_8(g(\chi))^{\frac{1}{2}}].$$

The constants c_j, $j = 6$–8, are listed in the Appendix and in $r(-\chi)$, $(g(-\chi))^{\frac{1}{2}} = (g(\chi))^{\frac{1}{2}}$. $R(\chi)$ can still be interpreted as a reflection coefficient on (I), as can $1/R(\chi)$ on (II).

The first objective is to find the mapping of the modal solution integration path $0 \leq \kappa \leq \infty$ onto the complex χ-plane. This is not trivial since it is determined by (5) or inversely by (6). As such, it involves the branches $\omega(\kappa)$ or $\eta(\chi)$ of the frequency equation.

If the branches $\omega(\kappa)$ are real for $0 \leq \kappa \leq \infty$, as can be expected, then it is helpful to observe that, by (6), ω/κ is real only on $|\chi| = 1$, the Re(χ)- and the Im(χ)-axes. Specifically, ω/κ is real on $\chi = e^{i\theta}$ only for $-\theta_{cr} \leq \theta \leq \theta_{cr}$ and $-\theta_{cr} \leq \theta - \pi \leq \theta_{cr}$ on both (I) and (II). On the Re(χ)-axis, ω/κ is real for all χ on (II) and for $(a-1)/(a+1) \leq |\chi| \leq (a+1)/(a-1)$ on (I). The constant a is given in the Appendix. The point $(a-1)/(a+1)$ along with its reciprocal, negative and negative reciprocal are zeros of κ, which are all on (I). Similarly ω has four zeros on (I). The Im(χ)-axis is of interest only for the lowest symmetrical and asymmetrical branches, and then only if the zeros of ω are on this axis.

As in the isotropic case, only the half disk

$$|\chi| \leq 1, \qquad \text{Im}(\chi) \geq 0 \tag{10}$$

need be considered for a complete understanding of the branches, and only $\chi = e^{i\theta}$, $0 \leq \theta \leq \pi$, and $-1 \leq \chi \leq 1$ appear to be possible integration paths for all but the lowest branches.

The following results are derived in [10] for the infinite set of branches $\eta(\chi)$ of (8) on the boundary of the half disk (10):

(a) If $-1 < R < 1$ and $-1 < \chi R < 1$, all branches are real.

(b) If $-1 < 1/R < 1$ and $-1 < \chi R < 1$, real multi-valued branches connected by complex loops are present.

(c) If $-1 < 1/R < 1$ and $-1 < 1/(\chi R) < 1$, both real and complex single-valued branches are present.

(d) If $|R| = 1$ and $|\chi| = 1$, two sets of branches are present, which take the forms

$$\eta(e^{i\theta}) = |\eta|\, e^{-i\theta/2}, \tag{11a}$$

called α_2 branches, and

$$\eta(e^{i\theta}) = i|\eta|\, e^{-i\theta/2}, \tag{11b}$$

called α_1 branches.

Thus, it merely takes an investigation of $R = R(\chi)$ to determine the form of the branches $\eta(\chi)$. These results are illustrated for a typical α_2 branch $\eta_n(\chi)$, $n = 1, 2, 3, \ldots$, in Fig. 1 along with its mapping into the κ, ω-plane as the branch $\omega_n(\kappa)$. The two lowest branches, $n = 0$, are not precisely of this form. No distinction is made between the symmetrical and asymmetrical branches in this notation.

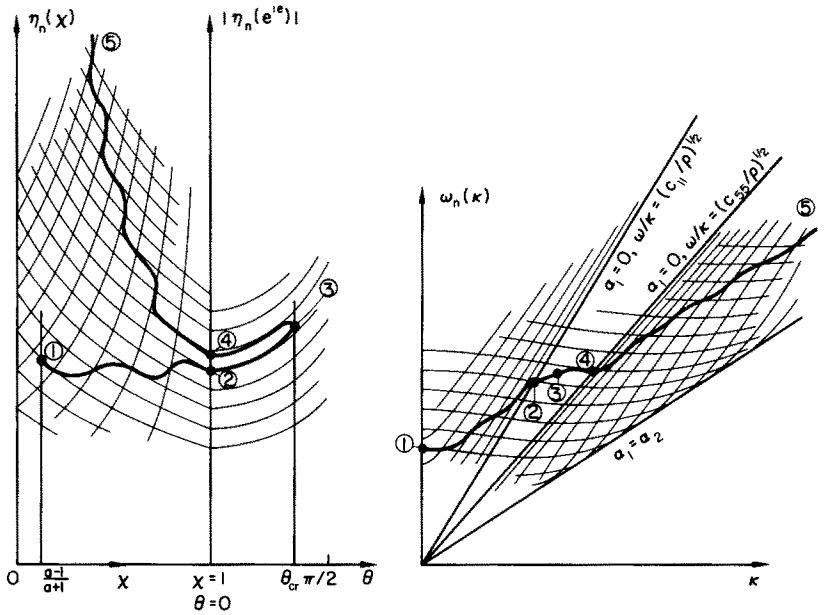

FIG. 1. A typical α_2 branch $\eta_n(\chi)$, $n = 1, 2, 3, \ldots$, and its mapping $\omega_n(\kappa)$ for $0 \leq \kappa \leq \infty$: ①–②–③, sheet (I); ③–④–⑤, sheet (II).

Of the conditions preceding (11a), (a) is satisfied on (I) for $(a-1)/(a+1) < \chi < 1$ with $R = 1$ at both end points. (d) is satisfied on $0 \leq \theta \leq \theta_{cr}$ on both (I) and (II) with

$$R(e^{i\theta}) = e^{i\gamma(\theta)}, \qquad \gamma(\theta) = 2\tan^{-1}[-ir(-e^{i\theta})/r(e^{i\theta})] \tag{12}$$

and $0 \leq \gamma(\theta) \leq \pi$ where $\gamma(0) = 0$ on (I) and $\gamma(0) = \pi$ on (II). There is a branch point on this branch at $\chi_{cr} = e^{i\theta_{cr}}$. The figure is drawn as if (b) is satisfied on (II) for $0 < \chi < 1$; however, (c) may also apply over some of this interval. This depends on the location of the point

$$\chi_0 = e^{i\theta_0}, \qquad \theta_0 = \tan^{-1}\left(\frac{2c_{13}\{c_{33}[c_{33}(c_{11}-c_{55})-c_{13}^2]\}^{\frac{1}{2}}}{c_{55}^{\frac{1}{2}}(c_{11}c_{33}+2c_{13}c_{33}-c_{13}^2)}\right) \tag{13}$$

where $\chi R(\chi) = -1$. This point moves off $\chi = e^{i\theta}$, $0 \leq \theta \leq \theta_{cr}$, and onto the Re($\chi$)-axis, $0 < \chi < 1$, for

$$c_{13}^2 > c_{33}(c_{11} - c_{55}). \tag{14}$$

If this is so, (b) is satisfied for $0 < \chi < \chi_0$ and (c) for $\chi_0 < \chi < 1$.

The subscript on χ_0 refers to the fact that this point is the zero of the lowest symmetrical branch $\eta_0(\chi)$. Hence, the low-frequency plate velocity is given by $\omega/\kappa|_{\chi=\chi_0}$ from (6). It is noted that the plate velocity is less than $(c_{55}/\rho)^{\frac{1}{2}}$ if (14) holds.

The numbers ①–⑤ in Fig. 1 label corresponding points on the branch $\eta_n(\chi)$ and its mapping $\omega_n(\kappa)$. The point χ_{cr} or ③ is seen to be a branch point only in the χ, η-space. Point ⑤ is meant to be the limiting point $\chi \to 0$ or $\kappa \to \infty$.

A partial grid made up of the curves $\alpha_j = p_j\pi/2H$, $p_j = 1, 2, 3, \ldots$, is shown in Fig. 1. These are hyperbolas, as they are for the isotropic case, in the χ, η-space; however, they are more complicated curves given by the algebraic functions (4) in the κ, ω-plane.

It is of interest that finite, real points common to $\alpha_2 = p_2\pi/2H$ and the line $\omega/\kappa = (c_{55}/\rho)^{\frac{1}{2}}$ exist only if (3) is satisfied. In which case, an α_2 curve finally becomes an α_1 curve on the line labeled $\alpha_1 = \alpha_2$ in Fig. 1 where $\omega/\kappa|_{\chi=0} < (c_{55}/\rho)^{\frac{1}{2}}$, given by (6) on (II). This corresponds to the radical in (4) vanishing, and, specifically, to the largest zero ω/κ of this radical.

Of similar interest is that the α_2 curves are concaved downward at $\kappa = 0$, as shown in Fig. 1, only if

$$(c_{13} + c_{55})^2 > c_{11}(c_{33} - c_{55}). \tag{15}$$

This is a counterpart to (3) and, by Musgrave [2], cusped wave fronts are to be expected about the x_3-axis in this case.

Some of these features in Fig. 1 are exaggerated in the κ, ω-plane. Specifically, the lines $\omega/\kappa = (c_{55}/\rho)^{\frac{1}{2}}$ and $\alpha_1 = \alpha_2$ are separated more than could be expected for most anisotropic solids. This is done to show more clearly how the grid and the branches map into this sector.

The asymptotic behavior of the branches, which approach the value $\omega/\kappa|_{\chi=0}$ just mentioned, is not smooth as $\kappa \to \infty$ [or $\chi \to 0$ on (II)]. The behavior of the branches is smooth only if (3) does not hold so that $\omega/\kappa \to (c_{55}/\rho)^{\frac{1}{2}}$. It has not been shown that the branches $\omega_n(\kappa)$ are single-valued; however, it is a good assumption that they are, but would be difficult to prove.

An infinite set of α_1 branches, satisfying (11b) on $\chi = e^{i\theta}$, $0 \leq \theta \leq \theta_{cr}$, also exists and they are denoted by $\eta_m(\chi)$ for both the symmetrical, $m = 0, 1, 2, \ldots$, and asymmetrical branches, $m = 1, 2, 3, \ldots$. Both κ and ω are pure imaginary on these branches for $\chi = e^{i\theta}$, $0 \leq \theta \leq \theta_{cr}$. The α_1 branches are unbounded at $\chi = 1$ ($\theta = 0$) on both (I) and (II) and they also have branch points at $\chi_{cr} = e^{i\theta_{cr}}$. On (I) they continue onto the real branches $\eta_n(\chi)$ on $(a-1)/(a+1) \leq \chi < 1$ by continuations like the dilatational continuations described in [1]. Similarly, on (II) they continue over the real branches and the complex loops connecting at the branch points on the Re(χ)-axis. The α_1 branches are not involved in the modal solution until it is replaced with a more convenient high-frequency form in Section 3, where these latter continuations are discussed in more detail.

The integration path C, consisting of the paths $C^{(I)}$ and $C^{(II)}$, is shown in Fig. 2. The fact that this is a mapping of $0 \leq \kappa \leq \infty$ for the branches $\omega_n(\kappa)$, $n = 1, 2, 3, \ldots$, results directly from Fig. 1. Since the branches $\eta_n(\chi)$ are multi-valued on $0 < \chi < 1$ on (II) [or on $0 < \chi < \chi_0$ if (14) holds], the branch points are encircled as shown on the right of Fig. 2. This gives the

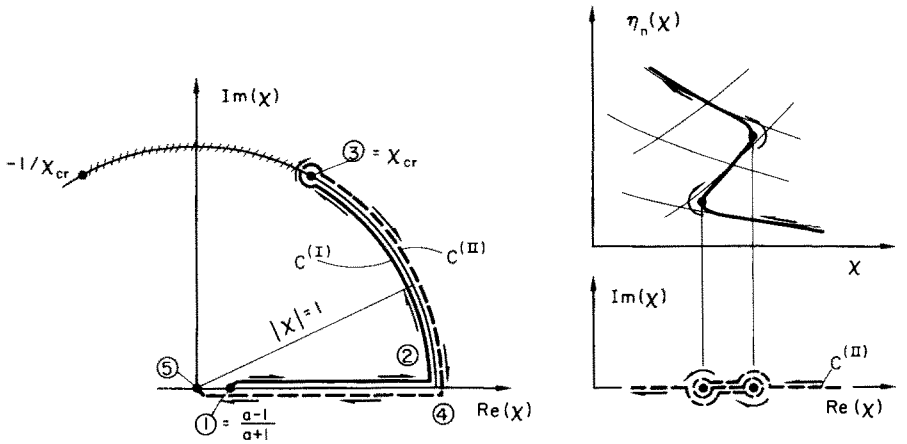

FIG. 2. Integration path $C = C^{(I)} + C^{(II)}$. Detail of $C^{(II)}$ and the accompanying continuation over a multi-valued branch: solid line, sheet (I); dashed line, sheet (II).

proper mapping indicated in Fig. 1. This feature makes the integration paths different for different branches, but only for $C^{(II)}$ on the Re(χ)-axis.

The solution of this problem is identically zero in the region beyond the front-running wave front in the plate, the form of which becomes clear in Section 5. In the remaining region, the modal solution in the χ, η variables is given by

$$\begin{pmatrix} u(x_1, x_3, t) \\ w(x_1, x_3, t) \end{pmatrix} = \frac{8I_0(c_{13}+c_{55})^2(c_{55}/\rho)^{\frac{1}{2}}}{\pi H c_{13}c_{55}(c_{11}-c_{55})} \sum_{n=0}^{\infty} \begin{pmatrix} u_{n(+)} + u_{n(-)} \\ w_{n(+)} - w_{n(-)} \end{pmatrix} \tag{16}$$

where

$$\begin{pmatrix} u_{n(\pm)} \\ w_{n(\pm)} \end{pmatrix} = \int_C \frac{\sin(\omega t)}{\cos(\eta) \pm \chi R(\chi) \cos(\chi\eta)} \begin{pmatrix} U(\chi)\sin(\kappa x_1)(\tilde{u}_{(\pm)1} - \tilde{u}_{(\pm)2}) \\ W(\chi)\cos(\kappa x_1)(\tilde{w}_{(\pm)1} - \tilde{w}_{(\pm)2}) \end{pmatrix} \Bigg|_{\eta=\eta_n(\chi)} \mathrm{d}\chi, \tag{17}$$

$$\left.\begin{aligned} \tilde{u}_{(+)j} &= f_j(\chi)\sin(\alpha_k H)\cos(\alpha_j x_3), \\ \tilde{u}_{(-)j} &= f_j(\chi)\cos(\alpha_k H)\sin(\alpha_j x_3), \\ \tilde{w}_{(+)j} &= h_j(\chi)\sin(\alpha_k H)\sin(\alpha_j x_3), \\ \tilde{w}_{(-)j} &= h_j(\chi)\cos(\alpha_k H)\cos(\alpha_j x_3), \end{aligned}\right\} \quad (j,k = 1,2;\ k \neq j)$$

$$f_j(\chi) = \frac{c_{13}(1+\chi)}{2(c_{13}+c_{55})[1-(-1)^j\chi]}\{[1-(-1)^j\chi]^2 + c_6(1+\chi^2) - c_6(g(\chi))^{\frac{1}{2}}\},$$

$$h_j(\chi) = \frac{c_{13}[1-(-1)^j\chi]}{(c_{13}+c_{55})(1-\chi)^2(1+\chi)}\{-c_{55}[1+(-1)^j\chi]^2/c_{13} + c_6(1+\chi^2) - c_6(g(\chi))^{\frac{1}{2}}\} f_j(\chi),$$

$$U(\chi) = \frac{\chi(1+\chi)(1-\chi)^2}{(g(\chi))^{\frac{1}{2}}[c_3(1+\chi^2) + c_4(g(\chi))^{\frac{1}{2}}]^{\frac{1}{2}}[r(\chi) - r(-\chi)]},$$

$$W(\chi) = \alpha_1 U(\chi)/\kappa = (1-\chi)U(\chi)/[c_1(1+\chi^2) + c_2(g(\chi))^{\frac{1}{2}}]^{\frac{1}{2}}.$$

The $(\pm)$ signs refer to symmetrical and asymmetrical waves as in (8); α_j, κ and ω are given by (6); the symmetrical and asymmetrical branches, both denoted by $\eta_n(\chi)$, $n = 0, 1, 2, \ldots$, satisfy (8), and are α_2 branches of the form (11a) on $\chi = e^{i\theta}$; and the integration paths C are shown in Fig. 2 except for the lowest branches, $n = 0$, which are not of interest here.

If (3) does not hold, the integration path C is exactly the same as for the isotropic case [1], running from $(a-1)/(a+1)$ to $\chi = 1$ and then to $\chi = -1$ on $\chi = e^{i\theta}$, $0 \leq \theta \leq \pi$. The path actually terminates at $\chi = i$ for the special case of an equality in (3). Another exception, which also does not lead to complications, occurs if $(c_{13}+c_{55})^2 < \frac{1}{2}(c_{33}-c_{55})(c_{11}-c_{55})$ so that the zero $(a-1)/(a+1)$ of κ moves onto the second sheet and slightly alters the beginning part of C. The method described in [1] can be used to obtain high-frequency approximations even for anisotropic materials with (15) applying, so that cusped wave fronts exist about the x_3-axis, and for materials such as beryl crystals, treated by Kraut [3], in which wave fronts occur with cusps free of the coordinate axes (axes of symmetry).

3. THE MODAL SOLUTION ON THE α_1 AND α_2 BRANCHES

By symmetry, only half of the plate need be considered. The modal solution which follows is valid only for the response of the right half, $x_1 \geq 0$, of the plate except for the response associated with wave fronts which have cusps extending into $x_1 < 0$.

For the proposed method to succeed, (17) must be written in a special form. Otherwise, convergence is lost and clearly incorrect answers result. Thus, the integrals in (17) are written as

$$\begin{aligned}\begin{pmatrix} u_{n(\pm)} \\ w_{n(\pm)} \end{pmatrix} = \begin{pmatrix} \mathrm{Im} \\ \mathrm{Re} \end{pmatrix} \Bigg\{ & \int_{C^{(\mathrm{I})}+C^{(\mathrm{II})}} \begin{pmatrix} U_1(\chi,\eta,x_3,t) \\ W_1(\chi,\eta,x_3,t) \end{pmatrix} e^{i\kappa x_1} \Big|_{\eta=\eta_n(\chi)} d\chi \\ & + \int_{C^{(\mathrm{I})}} \begin{pmatrix} U_2^{(\mathrm{I})}(\chi,\eta,x_1,x_3) \\ W_2^{(\mathrm{I})}(\chi,\eta,x_1,x_3) \end{pmatrix} e^{i\omega t} \Big|_{\eta=\eta_n(\chi)} d\chi \\ & + \int_{C^{(\mathrm{II})}} \begin{pmatrix} U_2^{(\mathrm{II})}(\chi,\eta,x_3,t) \\ W_2^{(\mathrm{II})}(\chi,\eta,x_3,t) \end{pmatrix} e^{i\kappa x_1} \Big|_{\eta=\eta_n(\chi)} d\chi \Bigg\} \end{aligned} \tag{18}$$

with $C^{(\mathrm{I})}$ and $C^{(\mathrm{II})}$ shown in Fig. 2. The first integral is associated with α_1 through $\tilde{u}_{(\pm)1}$ and $\tilde{w}_{(\pm)1}$ and the last two integrals are associated with α_2 through $\tilde{u}_{(\pm)2}$ and $\tilde{w}_{(\pm)2}$. Thus, the functions U_1, W_1, $U_2^{(\mathrm{I})}$, etc., are obtained directly from (17). For simplicity of notation, the subscripts $(\pm)$ are dropped from these functions.

Using the notation in (18), the modal solution on the α_1 and α_2 branches, with u and w still given by (16), is

$$\begin{aligned}\sum_{n=1}^{\infty} \begin{pmatrix} u_{n(\pm)} \\ w_{n(\pm)} \end{pmatrix} = \begin{pmatrix} \mathrm{Im} \\ \mathrm{Re} \end{pmatrix} \Bigg\{ & \sum_{n=1}^{\infty} \int_{C_2^{(\mathrm{II})}} \left[\begin{pmatrix} U_1 \\ W_1 \end{pmatrix} e^{i\kappa x_1} + \begin{pmatrix} U_2^{(\mathrm{I})} \\ W_2^{(\mathrm{I})} \end{pmatrix} e^{i\omega t} \right] \Big|_{\eta=\eta_n(\chi)} d\chi \\ & + \sum_{m=0,1}^{\infty} \int_{C_1^{(\mathrm{I})}} \left[\begin{pmatrix} U_1 \\ W_1 \end{pmatrix} e^{i\kappa x_1} + \begin{pmatrix} U_2^{(\mathrm{I})} \\ W_2^{(\mathrm{I})} \end{pmatrix} e^{i\omega t} \right] \Big|_{\eta=\eta_m(\chi)} d\chi \\ & + \sum_{n=1}^{\infty} \int_{C_2^{(\mathrm{II})}} \left[\begin{pmatrix} -U_1 \\ W_1 \end{pmatrix} e^{-i\kappa x_1} + \begin{pmatrix} U_2^{(\mathrm{II})} \\ W_2^{(\mathrm{II})} \end{pmatrix} e^{i\kappa x_1} \right] \Big|_{\eta=\eta_n(\chi)} d\chi \\ & + \sum_{m=0,1}^{\infty} \int_{C_1^{(\mathrm{II})}} \left[\begin{pmatrix} U_1 \\ W_1 \end{pmatrix} e^{i\kappa x_1} + \begin{pmatrix} -U_2^{(\mathrm{II})} \\ W_2^{(\mathrm{II})} \end{pmatrix} e^{-i\kappa x_1} \right] \Big|_{\eta=\eta_m(\chi)} d\chi \Bigg\}. \end{aligned} \tag{19}$$

The lowest symmetrical and asymmetrical modes, $n = 0$, are not included here and they can be evaluated by other, less complicated means. The branches $\eta_n(\chi)$ and $\eta_m(\chi)$ are the α_2 and α_1 branches and their analytic continuations and the branch $m = 0$ is involved only for the symmetrical case. The integration paths in (19) are shown in Fig. 3. $C_2^{(I)}$ and $C_1^{(I)}$ run from $(a-1)/(a+1)$ to χ_{cr} in any manner such that they remain to the left and right of certain sets of branch points of the branches over which the integration is being carried out. The isotropic case [1] is referred to for details of similar branch points and paths of integration. Both $C_2^{(II)}$ and $C_1^{(II)}$ must remain to the right of any branch points of their branches on (II) of the half disk (10). All other branch points are on $0 < \chi < 1$ unless (14) holds, in which case, these paths should be to the left of them.

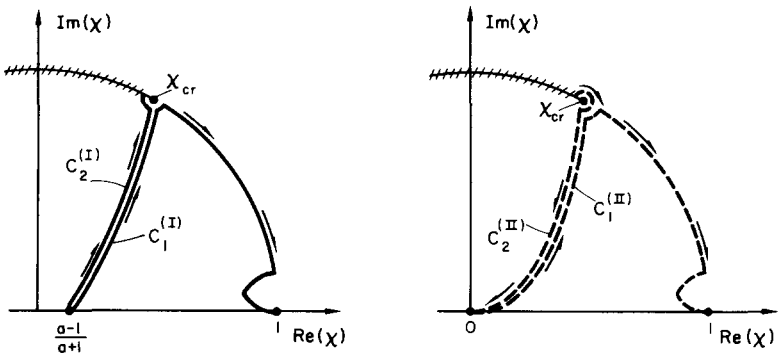

FIG. 3. New integration paths: solid lines, sheet (I); dashed lines, sheet (II).

The equivalence of this modal solution (19) and the original form (16) is argued in the same way as was done for the isotropic case [1]. The new form is shown to be a rearrangement of the original form.

The first two integrals in (19) are equivalent to the part of (16) resulting from integration over $C^{(I)}$ by almost exactly the same argument as for the isotropic case, which is not repeated here.

The paths $C_2^{(II)}$ and $C_1^{(II)}$ are deformed onto $0 \leq \chi \leq 1$ with indentions for branch points. Deformed $C_2^{(II)}$ then continues from $\chi = 1$ to χ_{cr} on $\chi = e^{i\theta}$, $0 \leq \theta \leq \theta_{cr}$, and the integration is over the α_2 branches exactly as in (16) for the part of $C^{(II)}$ which is on this segment. On $0 \leq \chi \leq 1$ these integrals must add together in such a way as to just leave integrations over the real, multi-valued branches $\eta(\chi)$ shown in Fig. 1. This is the case, and it is explained by referring to Fig. 4, showing a typical situation involving two branch points and a complex connecting loop on $0 < \chi < 1$ [on $0 < \chi < \chi_0$ if (14) holds]. Deformed $C_1^{(II)}$ carries its branch [an analytic continuation of an α_1 branch $\eta_m(\chi)$] over real values and complex values with $\mathrm{Im}(\eta) > 0$ (positive half of the loops). Likewise, deformed $C_2^{(II)}$ carries its branch [an analytic continuation of an α_2 branch $\eta_n(\chi)$] over real values and complex values with $\mathrm{Im}(\eta) < 0$ (negative half of the loops). Every loop is covered as shown in Fig. 4, and a simple calculation, using the fact that $\eta_n^*(\chi) = \eta_m(\chi)$ (* denotes complex conjugate) on this loop and that U_1, W_1, $U_2^{(II)}$ and $W_2^{(II)}$ are all real for χ and η real, shows that these integrals cancel on the loops. Thus, precisely the correct integrations over the real branches on $0 < \chi < 1$ remain.

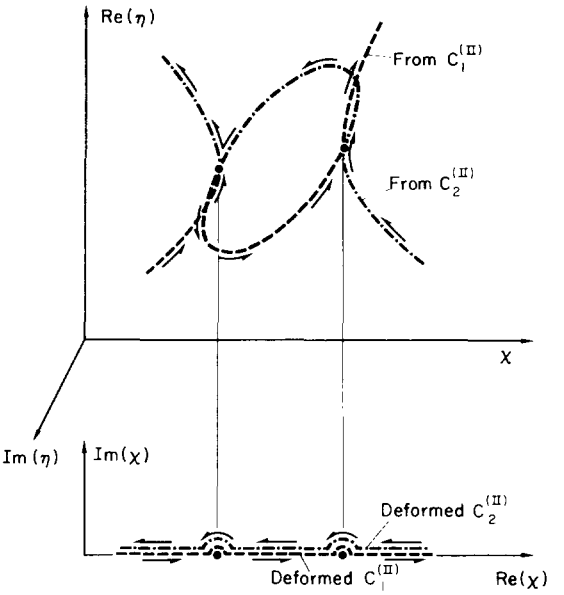

FIG. 4.

For (14) holding and $\chi_0 < \chi < 1$, these branch points are off the Re(χ)-axis with half of them being interior to the half disk (10). The equivalence follows similarly with the additional cancellation on the branch line integrals.

Collecting these results, the solution (19) is equivalent to the original modal solution (16) by deforming paths of integration and rearranging parts of the integrations and summations.

4. THE HIGH-FREQUENCY APPROXIMATION

Another reason that the form (8) of the frequency equation is fortunate is that series representations for the branches, given in [1], are valid here. The dependence there on $R(\chi)$ is arbitrary and (9) can be used in those series. The α_2 branches correspond to the equivoluminal branches and the α_1 branches to the dilatational branches. Convergence follows from the isotropic case and the branch points at χ_{cr} do not alter convergence since they enter through $R(\chi)$. Thus, uniform convergence with respect to $\chi = e^{i\theta}$, $0 \leq \theta \leq \theta_{cr}$, on (I) and (II) is assured on any closed segment with $\theta = 0$ excluded for the α_2 branches. As in the isotropic case, the lowest symmetrical branches, $n = 0$ and $m = 0$, share a branch point at χ_0 given by (13) so that their series converge on somewhat smaller segments. Convergence off $\chi = e^{i\theta}$ is a much more difficult question. However, the region of convergence is still determined by the location of branch points of the branches. These branch points can be shown to move closer and closer to the Re(χ)-axis as the branch numbers n and m increase, at least near $(a-1)/(a+1)$ on (I) and $\chi = 0$ on (II), which are end points for the integration paths in (19).

Thus, these series representations are appropriate to use for a very accurate high-frequency approximation of the modal solution (19). Rather than list the details of the approximate integrals which result, as was done in [1], some of the steps in the derivation are given and certain of the results are discussed.

As in the isotropic case [1], the important terms (those which contain singular wave fronts) in (19) are those associated with α_j, denoted by the subscript on U_1, $U_2^{(\mathrm{II})}$, etc., with the integration over the corresponding α_j branches. These are the second term in the first integral, the first term in the second integral, the second term in the third integral and the first term in the fourth integral. The integrals are labeled $I_{22}^{(\mathrm{I})}$, $I_{11}^{(\mathrm{I})}$, $I_{22}^{(\mathrm{II})}$ and $I_{11}^{(\mathrm{II})}$, respectively. For example,

$$I_{22}^{(\mathrm{I})} = \begin{pmatrix} \mathrm{Im} \\ \mathrm{Re} \end{pmatrix} \sum_{n=1}^{\infty} \int_{C_2^{(\mathrm{I})}} \begin{pmatrix} U_2^{(\mathrm{I})} \\ W_2^{(\mathrm{I})} \end{pmatrix} \mathrm{e}^{i\omega t} \Big|_{\eta=\eta_n(\chi)} \mathrm{d}\chi.$$

After these integrals are approximated and the symmetrical and asymmetrical parts are added, they correspond closely with those in [1] as follows: $I_{22}^{(\mathrm{I})} + I_{22}^{(\mathrm{II})}$ with I_{ee} and $I_{11}^{(\mathrm{I})}$ with I_{dd}, while $I_{11}^{(\mathrm{II})}$ has no counterpart in the isotropic case or in any anisotropic case where (3) does not hold. The other four integrals in (19) are not zero; however, all of their singularities are canceled by the integrals just mentioned. Thus, they are not involved in representations for the singular wave fronts.

Phase functions are defined as

$$\begin{aligned} \Psi_\ell(x_1, x_3, t, \chi) &= \begin{cases} [\omega t - (-1)^\ell \kappa x_1 \pm \alpha_1 H + \alpha_2 x_3]/\eta & \text{on (I)} \\ [\kappa x_1 - (-1)^\ell \omega t \pm \alpha_1 H + \alpha_2 x_3]/\eta & \text{on (II)}, \end{cases} \\ \Phi_\ell(x_1, x_3, t, \chi) &= [\kappa x_1 - (-1)^\ell \omega t + \alpha_1 x_3 \pm \alpha_2 H]/\eta \qquad \text{on (I) and (II)} \end{aligned} \tag{20}$$

where the upper signs apply for $\ell = 1$-4, the lower signs for $\ell = 5$–8 and x_3 is replaced with $-x_3$ for $\ell = 3, 4, 7, 8$. Then, for example, from symmetrical $U_2^{(\mathrm{I})} \mathrm{e}^{i\omega t}$, terms containing exponential functions can be written as

$$\sin(\kappa x_1) \sin(\alpha_1 H) \cos(\alpha_2 x_3) \mathrm{e}^{i\omega t} = \frac{1}{8} \sum_{\ell=1}^{8} S_{1\ell} \mathrm{e}^{i\eta\Psi_\ell}$$

where $(S_{1\ell}) = (-1, 1, -1, 1, 1, -1, 1, -1)$.

The parts of the integrands in (19) containing the branches $\eta(\chi)$ are expanded using the following series representations from [10] (Φ_ℓ can be replaced with Ψ_ℓ throughout). The series

$$\frac{\mathrm{e}^{i\eta\Phi_\ell}}{\cos(\eta) + \chi R(\chi) \cos(\chi\eta)} \Big|_{\eta=\eta_n(\chi)} = \frac{2}{1+\chi} \sum_{p,q=0}^{\infty} A_{pq}(\chi, \Phi_\ell) \mathrm{e}^{iE_n^{(0)}(\chi)[\Phi_\ell - 1 - (1-\chi)p - 2q]} \tag{21}$$

is for the symmetrical α_2 branches, $n = 1, 2, 3, \ldots$, where $E_n^{(0)}(\chi) = \{2n\pi - i \log[R(\chi)]\}/(1+\chi)$ and $A_{pq}(\chi, \Phi)$ are given in [1]. The series for $\mathrm{e}^{i\eta\Phi_\ell}/[\cos(\eta) - \chi R(\chi) \cos(\chi\eta)]$, where $\eta = \eta_n(\chi)$, $n = 1, 2, 3, \ldots$, are the asymmetrical α_2 branches, is given by (21) with A_{pq} replaced with $(-1)^p A_{pq}$ and $E_n^{(0)}$ with $E_{n-\frac{1}{2}}^{(0)}$. Similarly,

$$\frac{\mathrm{e}^{i\eta\Phi_\ell}}{\cos(\eta) + \chi R(\chi) \cos(\chi\eta)} \Big|_{\eta=\eta_m(\chi)} = \frac{2}{1-\chi} \sum_{p,q=0}^{\infty} A'_{pq}(\chi, \Phi_\ell) \mathrm{e}^{iD_m^{(0)}(\chi)[\Phi_\ell + 1 + (1+\chi)p + 2q]} \tag{22}$$

is for the symmetrical α_1 branches, $m = 0, 1, 2, \ldots$, where $D_m^{(0)}(\chi) = \{(2m+1)\pi + i \log[R(\chi)]\}/(1-\chi)$ and $A'_{pq}(\chi, \Phi)$ result from [1]. The series for $e^{i\eta\Phi_\ell}/[\cos(\eta) - \chi R(\chi)\cos(\chi\eta)]$, where $\eta = \eta_m(\chi)$, $m = 1, 2, 3, \ldots$, are the asymmetrical α_1 branches, is given by (22) with A'_{pq} replaced with $(-1)^p A'_{pq}$ and $D_m^{(0)}$ with $D_{m-\frac{1}{2}}^{(0)}$.

These series can be expected to converge uniformly with respect to χ on the same regions on which the series for the branches $\eta(\chi)$ converge. This is true since the branch points are identified as simultaneous zeros of (8) and the terms $\cos(\eta) \pm \chi R(\chi)\cos(\chi\eta)$ (see [10]) and their location still determines the regions of convergence.

These series are used in (19) and the double summation on p and q is brought outside the integrals. The paths of integration on the resulting term-by-term integrals are then deformed as follows: $C_2^{(I)} + C_2^{(II)}$ is deformed back onto the original path C in Fig. 2 and $C_1^{(I)}$ and $C_1^{(II)}$ are both collapsed onto the Re(χ)-axis. Singularities arising from zeros of $R(\chi)$ through $\log[R(\chi)]$ are still a problem, as in the isotropic case [1], but they seem to defy analysis, and, on this point, the approximate solution will have to stand on the validity of the final results.

This being done, and with the extended phase functions

$$\begin{aligned} \Psi_{\ell pq} &= 2[\Psi_\ell - 1 - (1-\chi)p - 2q]/(1+\chi), \\ \Phi_{\ell pq} &= 2[\Phi_\ell + 1 + (1+\chi)p + 2q]/(1-\chi) \end{aligned} \tag{23}$$

defined, the summations over the mode numbers n and m are brought inside the integrals and carried out by using

$$\sum_{n=1}^{\infty} e^{in\pi\Phi} = -\frac{1}{2} + \sum_{m=-\infty}^{\infty} \delta(\Phi - 2m) + \frac{i}{2}\cot\left(\frac{\pi}{2}\Phi\right) \tag{24}$$

for $\Phi = \Phi_{\ell pq}, \Psi_{\ell pq}$ real. This is always true except for some cases on $\chi = e^{i\theta}$ where $\mathrm{Im}(\Psi_{\ell pq}) > 0$ and (24) is summed as a geometric series. All quantities in (19) can be summed in this way, even though the emphasis here is only on the singular terms.

The result of these calculations is a sum of integrals over $p, q = 1, 2, 3, \ldots$ and $\ell = 1$–8, similar to those derived in [1], some of which contain the wave-front singularities. The integrals are appropriate for numerical evaluation or for approximation near the wave fronts. Also, just a few of the integrals give an excellent high-frequency approximation for the response of the plate for early times when there are few wave fronts present.

5. THE GEOMETRY OF THE WAVE FRONTS

With $\Phi = \Phi_{\ell pq}, \Psi_{\ell pq}$ from (23) replacing χ or θ as the integration variable, the condition for a singular wave front is the simultaneous satisfaction of

$$\Phi = 2m, \qquad \frac{d\Phi}{d\chi} = 0 \tag{25}$$

for any integer m such that Φ is in the range of integration. The first of (25) gives the singular points of the generalized functions in (24) and the second gives an additional singularity in these integrals. When these coincide, as indicated by (25), the integrals fail to exist giving rise to a wave front singularity. The second of (25) is satisfied only for ℓ even, except for a few cusped wave fronts extending into $x_1 \geq 0$, which are mirror images of terms with ℓ even. Thus, only terms with ℓ even are considered.

Parametric equations for the wave fronts are given by (25) with χ, ℓ, p and q being the parameters. In order to investigate (25), the dimensionless quantities

$$\begin{aligned} L &= x_1(\rho/c_{55})^{\frac{1}{2}}/t, \\ Z^{(j)}_{\ell pq} &= [(2p+2q+1)H-(-1)^j x_3](\rho/c_{55})^{\frac{1}{2}}/t, \\ Q^{(j)}_{\ell pq} &= [2p+2q+1\mp(-1)^j]H(\rho/c_{55})^{\frac{1}{2}}/t \end{aligned} \tag{26}$$

are defined where $j = 1, 2$ refers to terms associated with the α_1 and α_2 branches. The comments regarding the $(\pm)$ signs and the sign of x_3 following (20) also apply here for $\ell = 2, 4, 6, 8$. To simplify notation, wave fronts from the various integrals will sometimes be identified by the parameter

$$Q_j = t(c_{55}/\rho)^{\frac{1}{2}}Q^{(j)}_{\ell pq}/H = 2p+2q+1\mp(-1)^j \tag{27}$$

rather than $Q^{(j)}_{\ell pq}$, and the sheet numbers will be affixed to this parameter, as $Q^{(\mathrm{I})}_j$ and $Q^{(\mathrm{II})}_j$.

The parametric equations (25) for the α_2 wave fronts contained in $I^{(\mathrm{I})}_{22}$ and $I^{(\mathrm{II})}_{22}$ become

$$\begin{aligned} L &= F_1(\chi)\pm F_2(\chi)Q^{(2)}_{\ell pq}, \\ Z^{(2)}_{\ell mq} &= \pm F_3(\chi)+F_4(\chi)Q^{(2)}_{\ell pq}, \end{aligned} \tag{28}$$

resulting from $\Psi_{\ell pq}$ with the upper sign on (I) and the lower on (II). The functions $F_j(\chi)$, $j = 1$–4, are listed in the Appendix.

It is significant that the parametric equations (25) for the α_1 wave fronts contained in $I^{(\mathrm{I})}_{11}$ and $I^{(\mathrm{II})}_{11}$ and resulting from $\Phi_{\ell pq}$ on both (I) and (II) can be obtained from (28) on (I) by making the changes $Q^{(2)}_{\ell pq} \to Z^{(1)}_{\ell -mq}$ and $Z^{(2)}_{\ell mq} \to Q^{(1)}_{\ell pq}$. This results in

$$\begin{aligned} L &= [F_1(\chi)F_4(\chi)-F_2(\chi)F_3(\chi)+F_2(\chi)Q^{(1)}_{\ell pq}]/F_4(\chi) \\ &= F_1(-\chi)+F_2(-\chi)Q^{(1)}_{\ell pq}, \\ Z^{(1)}_{\ell -mq} &= [-F_3(\chi)+Q^{(1)}_{\ell pq}]/F_4(\chi) \\ &= F_3(-\chi)+F_4(-\chi)Q^{(1)}_{\ell pq}. \end{aligned} \tag{29}$$

The form involving $F_j(-\chi)$ just results from properties of these functions and is listed only as a convenient, compact set of equations.

As a result of this interesting relationship between (28) and (29), the geometry of all wave fronts in the plate is derivable from a surface in the L, $Z^{(2)}_{\ell mq}$, $Q^{(2)}_{\ell pq}$-space given by (28) or, equivalently, in the L, $Q^{(1)}_{\ell pq}$, $Z^{(1)}_{\ell -mq}$-space given by (29). This surface is shown in Fig. 5. The small interior cusped part of the surface results from sheet (II) and is present only if (3) holds. Similarly, the cusped part of the surface in the foreground is present only if (15) holds. The α_1 wave fronts, shown as solid lines, result from vertical slices through this surface; while the α_2 wave fronts, shown as dashed lines, result from horizontal slices of the same thickness. The thickness is inversely proportional to the time, resulting in more wave fronts in the plate at later times, as expected. This vividly illustrates the coupling of the α_1 and α_2 wave fronts due to reflections at the plate faces, and the possibility of many cusped wave fronts.

These wave fronts are shown in the plate in Fig. 6. The parameters $Q^{(\mathrm{I})}_j$ and $Q^{(\mathrm{II})}_j$, defined by (27), identify these as α_j wave fronts from sheet (I) or (II). For example, the wave fronts $Q^{(\mathrm{I})}_2$ result from the response contained in the integral $I^{(\mathrm{I})}_{22}$. The figure is drawn with successive

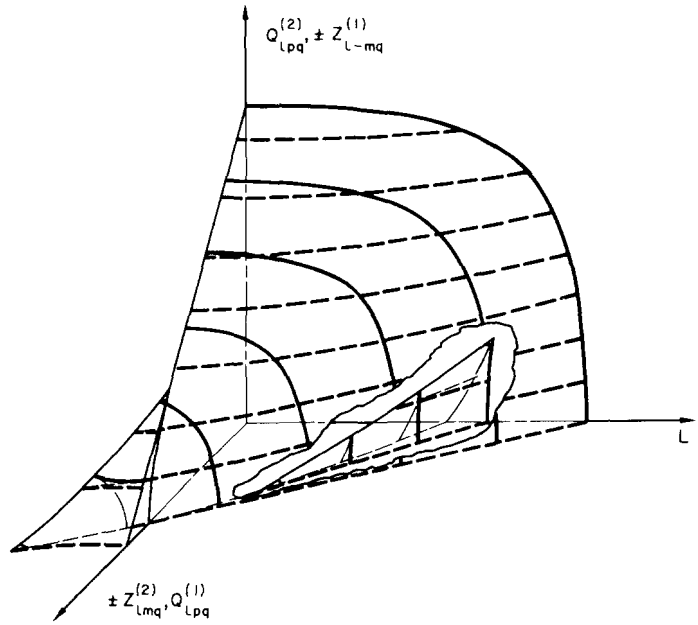

FIG. 5. Surface containing the wave fronts: upper signs, sheet (I); lower signs, sheet (II).

thicknesses of the plate repeated so that the wave fronts appear as smooth lines. The horizontal lines represent the faces $x_3 = \pm H$ of the plate and the figure should be folded as an accordion at these lines to visualize all of the wave fronts in a single plate thickness. The figure is drawn at a rather late time when many wave fronts are present, not to complicate the situation, but to insure that certain interesting wave fronts are present in the plate.

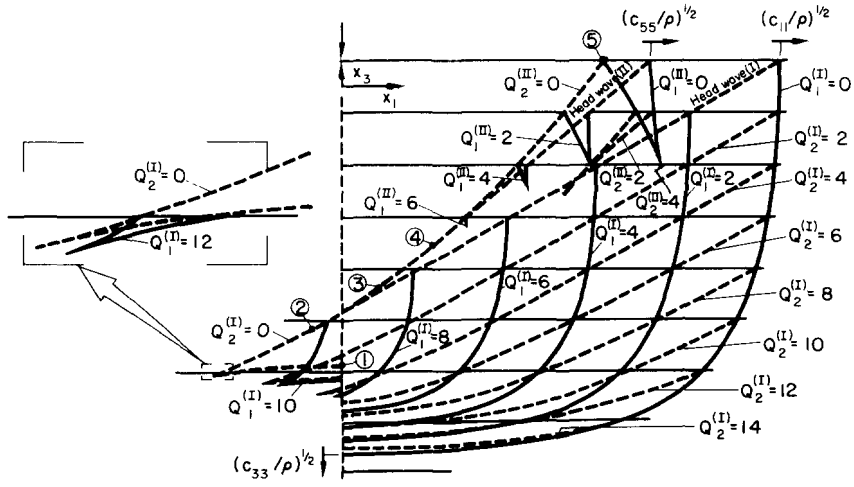

FIG. 6. Wave fronts at $t = 2H(\rho/c_{55})^{\frac{1}{2}}/0{\cdot}17$ for $c_{11} = 6$, $c_{33} = 5$, $c_{13} = c_{55} = 3$: solid lines, α_1 fronts; dashed lines, α_2 fronts.

The head waves (I) and (II) are not singular for the displacement resulting from the loading (2); however, they are shown in Fig. 6 (and in Fig. 5) and they result from $\Psi_{\ell 00} = 2m$, $\ell = 2, 4$, at the single point $\chi = 1$. Both waves are associated with the factor $1-\chi$ in the modal solution. Head wave (I) is just a generalization of the familiar isotropic head wave. However, head wave (II) is present only if (3) is satisfied. Head wave (II) occurs in the simpler half-space problem and it was studied by Kraut [11].

New results contained in Fig. 6 concern the multitude of cusped wave fronts. Reflected α_1 wave fronts always originally have cusps about the x_3-axis ($Q_1^{(I)} = 8, 10, 12$), and after a sufficient amount of time these cusps disappear ($Q_1^{(I)} = 2, 4, 6$). The reflected α_2 wave fronts do not have cusps about the x_3-axis at first ($Q_2^{(I)} = 6, 8, 10, 12, 14$), but they always finally develop cusps ($Q_2^{(I)} = 2, 4$). The enlargement of the tip of the cusp of $Q_2^{(I)} = 0$ on the left shows how a reflected α_1 wave front, $Q_1^{(I)} = 12$, begins. It has a mirror image on the right of $x_1 = 0$ and they will subsequently join together at $x_1 = 0$ as has $Q_1^{(I)} = 10$. $Q_2^{(II)} = 0$ reflects cusped α_1 wave fronts ($Q_1^{(II)} = 2, 4, 6$) at the plate faces and these along with $Q_1^{(II)} = 0$ reflect cusped α_2 wave fronts ($Q_2^{(II)} = 2, 4$).

Only the primary α_2 wave front, labeled both as $Q_2^{(I)} = 0$ and $Q_2^{(II)} = 0$, is numbered ①–⑤ corresponding to the points in Figs. 1 and 2. Thus, ①–③ is $Q_2^{(I)} = 0$ and ③–⑤ is $Q_2^{(II)} = 0$.

Velocities of three points on $x_3 = H$ and $x_1 = 0$ on the primary wave fronts $Q_2^{(I)} = 0$ and $Q_2^{(II)} = 0$, $Q_1^{(I)} = 0$, and $Q_1^{(II)} = 0$ are indicated in Fig. 6. In addition, point ① has velocity $(c_{55}/\rho)^{\frac{1}{2}}$. These waves, along with the two head waves, would be present in a half space $x_3 \leq H$. The unreflected portion of $Q_1^{(I)} = 0$ is the front-running wave front in the plate, mentioned in connection with the modal solution (16). The point ⑤ has velocity $\omega/\kappa|_{\chi=0}$ given by (6) on (II), which was discussed in Section 2.

6. WAVE-FRONT APPROXIMATIONS

A typical displacement integral is approximated near a singular wave front both near to and away from a cusp tip. This is done to show the method of approximation and the order of the singularities.

Only the integrals $I_{22}^{(I)}$ on ②–③ of $Q_2^{(I)} = 0$ and $I_{22}^{(II)}$ on ③–④ of $Q_2^{(II)} = 0$ in Fig. 6 contain the Dirac delta functions from (24) and, therefore, can be integrated directly. A $-\frac{1}{2}$ displacement singularity is predicted as ②–③–④ is approached from the front (right) side. This portion is a two-sided wave front, which is a generalization of the two-sided equivoluminal wave front in the isotropic case [1]. That work is referred to for evaluation of these integrals.

All other singular integrals result from the cotangent function in (24) and, adding the symmetrical and asymmetrical parts, half of the singularities cancel leaving $\cot[(\pi/4)\Phi]$ or $\tan[(\pi/4)\Phi]$ terms in the integrands. Thus, a typical displacement integral is

$$I = \text{P.V.} \int F(\chi) \cot\left(\frac{\pi}{4}\Phi\right) d\chi \tag{30}$$

where the smooth functions $F(\chi)$ result from the previous integrals. This is a Cauchy principal value integral due to the simple poles at $\Phi = 4m$. In fact, the wave-front singularities are identified with values of x_1, x_3, t for which these poles are not simple and (30) fails to exist

even as a principal value. There is really no reason to use Φ as the integration variable for these approximations. The limits of integration are left indefinite and are meant to include no more than one pair of singularities $\Phi = 4m$ for some fixed integer m.

For purposes of discussion, it will be assumed that the response contained in $I_{11}^{(II)}$ and associated with the wave front $Q_1^{(II)} = 0$ in Fig. 6 is to be approximated. Therefore, $\Phi = \Phi_{\ell 00}$ in (30) with $\ell = 8$ giving the odd reflections. These arise from singularities at $\Phi = 4, 8, 12, \ldots$. The $\ell = 6$ terms have $\tan[(\pi/4)\Phi]$ in the integrands and give the unreflected portion and all even reflections from singularities at $\Phi = 2, 6, 10, \ldots$.

The first approximation of (30) is made away from a cusp tip. Using the notation

$$\Phi_c^{(n)} = \left.\frac{d^n\Phi}{d\chi^n}\right|_{\chi=\chi_c},$$

χ_c is defined by making $\Phi_c' = 0$. It is assumed that Φ_c'' is finite (if it is infinitesimal, a cusp tip will be found to be nearby) and the approximation

$$\cot\left(\frac{\pi}{4}\Phi\right) \cong \frac{4}{\pi}[\Phi_c - 4m + \tfrac{1}{2}\Phi_c''(\chi-\chi_c)^2]^{-1}$$

is used for $\Phi_c - 4m$ small. Further, $F(\chi)$ is approximated with $F_c = F(\chi_c)|_{\Phi_c = 4m}$ (the value at the wave front), and the approximation of (30) is

$$I \cong \begin{cases} 4F_c[\tfrac{1}{2}(\Phi_c-4m)\Phi_c'']^{-\frac{1}{2}}\operatorname{sgn}(\Phi_c-4m) = O(|\Phi_c-4m|^{-\frac{1}{2}}) & \text{for} \quad (\Phi_c-4m)\Phi_c'' > 0 \\ O(1) \quad \text{for} \quad (\Phi_c-4m)\Phi_c'' < 0 \end{cases} \tag{31}$$

for $\Phi_c - 4m$ small.

Before (31) is discussed, the approximation near a cusp tip is given. It can be shown from (29), or from (28), that if, in addition to (25), $\Phi'' = 0$ is required, then $dL/d\chi = dZ/d\chi = 0$ (the inverse also holds) for $Z = Z_{\ell -mq}^{(1)}, Z_{\ell mq}^{(2)}$. This is obviously the condition for a cusp tip since, geometrically, either or both L and Z must be stationary with respect to χ at the tip. χ_c is now defined by making $\Phi_c'' = 0$, and it is assumed that Φ_c''' is finite. The region of consideration is restricted to that surrounding the cusp tip, rather than that inside the tip. Proceeding similarly, except that

$$\cot\left(\frac{\pi}{4}\Phi\right) \cong \frac{4}{\pi}[\Phi_c - 4m + \Phi_c'(\chi-\chi_c) + \tfrac{1}{6}\Phi_c'''(\chi-\chi_c)^3]^{-1}$$

is now used, leads to the approximation

$$I \cong \frac{-72F_cA}{\Phi_c'''(3A^2 + 6\Phi_c'/\Phi_c''')(3A^2 + 24\Phi_c'/\Phi_c''')^{\frac{1}{2}}}, \tag{32}$$

$$A = [-3(\Phi_c-4m)/\Phi_c''' + B^{\frac{1}{2}}]^{\frac{1}{3}} - [3(\Phi_c-4m)/\Phi_c''' + B^{\frac{1}{2}}]^{\frac{1}{3}},$$

$$B = (3\Phi_c'/\Phi_c''')^3 + [3(\Phi_c-4m)/\Phi_c''']^2,$$

which is valid for $\Phi_c - 4m$ and Φ_c' small and for $B \geq 0$. (32) predicts $I = O(|\Phi_c - 4m|^{-\frac{1}{3}})$ except for the case $|\Phi_c - 4m| \ll |\Phi_c'|$. Regarding this case, $I = 0$ (to the order of this approximation) for $\Phi_c' \neq 0$ and $A = 0$, which implies that $\Phi_c = 4m$.

To interpret that result in the x_1, x_3, t variables, let $x_3 = f(x_1, t)$ represent the solution of (29) for $Q_{\ell pq}^{(1)} = 0$ so that it gives the curve $Q_1^{(II)} = 0$ in Fig. 6. Then it is a simple matter to show that $\partial\Phi_c/\partial x_3 \neq 0$ in both (31) and (32). Therefore, $\Phi_c - 4m$ is a linear function of

$x_3 - f(x_1, t)$ near the wave front and

$$O(|\Phi_c - 4m|) = O(|x_3 - f(x_1, t)|).$$

A sketch of level curves for a displacement component (either u or w) is shown in Fig. 7. The positive and negative signs depend on the sign of F_c and only the differing signs is meant to be emphasized here. The cusped wave front itself is labeled $\pm\infty$, it being singular for the loading (2). The wave front propagates from left to right and expands downward, as does $Q_1^{(II)} = 0$ in Fig. 6.

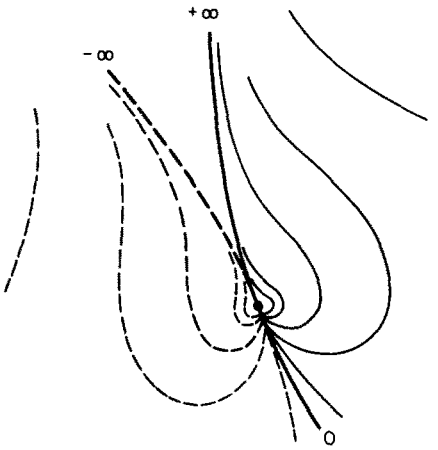

FIG. 7. Level displacement curves surrounding a cusp tip: solid lines, positive displacement; dashed lines, negative displacement.

The portion away from the cusp tip is singular in displacement like $O(|x_3 - f(x_1, t)|^{-\frac{1}{2}})$ from (31). This is much like the isotropic case, except that the front running portion on the right has its singularity *in front* of the wave front. That is, as the wave propagates past a fixed point x_1, x_3 the disturbance is felt *before* the wave front actually arrives. The trailing part of the wave front is of different sign and has its $-\frac{1}{2}$ displacement singularity following the front. The region interior to the cusp is $O(1)$ by (31).

From (32), the displacement is singular like $O(|x_3 - f(x_1, t)|^{-\frac{2}{3}})$ as the cusp tip is approached from any direction, except on the line determined by $\Phi' = \Phi'' = 0$, where it is zero. And, as seen in Fig. 7, this line divides positive and negative portions of the response. The cusp tip is thus a propagating line singularity of order $-\frac{2}{3}$, as reported by Kraut [3], for the line loading (2).

The term F_c in (31) and (32) contains

$$\exp\{-\tfrac{1}{2}\Phi_c \log[R(\chi_c)]\}|_{\Phi_c = 4m} = [R(\chi_c)]^{-2m}|_{\Phi_c = 4m}$$

for $\Phi_c = \Phi_{800}|_{\chi = \chi_c}$ and $m = 1, 2, 3, \ldots$. This is consistent with the interpretation of $1/R$ as the reflection coefficient on (II). This $\ell = 8$ term gives all odd reflections of $Q_1^{(II)} = 0$.

The $\ell = 6$ term has singularities at $\Phi_{600} = 4m-2$, $m = 1, 2, 3, \ldots$, and results in the factors $[R(\chi_c)]^{-2m+1}$ for the unreflected portion and all even reflections.

The response at a specific time and location in the plate is approximated by (31) and (32). In order to use the calculations leading to Fig. 6 and to have cusp tips involved, the response is considered at one half the time elapse in Fig. 6 on a portion of a fixed horizontal line near the lower plate face $x_3 = -H$. The two lowest modes, not included in (19), contribute a singular surface wave on the upper face $x_3 = H$ for the impulsive input (2). Thus, this response is more meaningful if this region is avoided. Of course, the surface wave response merely adds to any results obtained here.

A greatly magnified portion of the plate near the lower face is shown in Fig. 8, along with the wave fronts present. The fixed horizontal line $x_3 = -0{\cdot}89H$ is chosen to pass through a

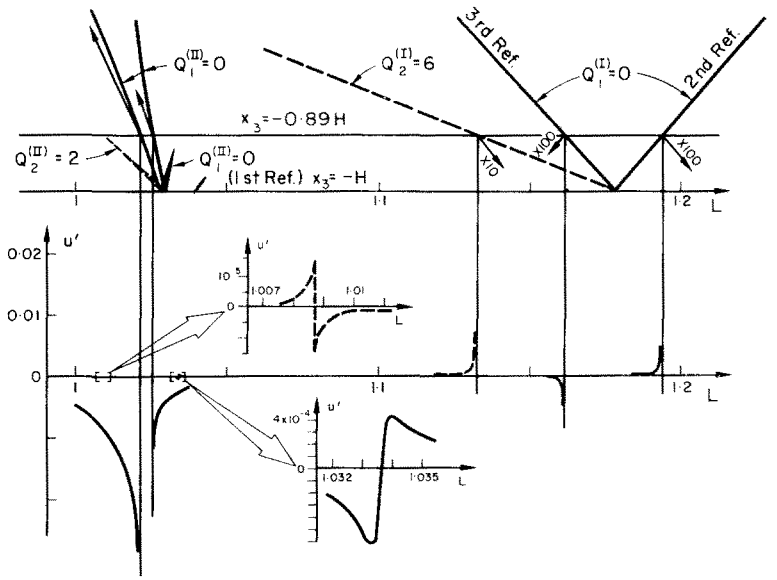

FIG. 8. Approximate response at $t = 2H(\rho/c_{55})^{\frac{1}{2}}/0{\cdot}34$ on a portion of the line $x_3 = -0{\cdot}89H$.

variety of wave fronts, and near to two cusp tips. In the isotropic case the first three wave fronts encountered from right to left would be denoted in terms of primary and secondary (dilatational and equivoluminal) waves as *PPP*, *PPPP* and *PPPS*. The dimensionless horizontal coordinate L is defined in (26).

The following equation defines the dimensionless displacement components u' and w' and gives the approximate integral representation, derived as suggested in Section 4, which contains all of the singularities corresponding to the wave fronts in Fig. 8.

$$\begin{pmatrix} u' \\ w' \end{pmatrix} = \frac{\pi H c_{13} c_{55}(c_{11}-c_{55})}{I_0(c_{13}+c_{55})^2(c_{55}/\rho)^{\frac{1}{2}}} \begin{pmatrix} u \\ w \end{pmatrix}$$

$Q_1^{(\mathrm{I})} = 0$ (2nd Ref.)
$m\ell pq = -2800$

$$\cong \text{P.V.} \int_{(a-1)/(a+1)}^{1} \begin{pmatrix} -Uf_1 \\ Wh_1 \end{pmatrix} \frac{\exp(-\frac{1}{2}\Phi_{800}\log R)\cot[(\pi/4)\Phi_{800}]}{1-\chi}\,d\chi$$

$Q_1^{(\mathrm{I})} = 0$ (3rd Ref.)
$m\ell pq = -3600$

$$-\text{P.V.} \int_{(a-1)/(a+1)}^{1} \begin{pmatrix} Uf_1 \\ Wh_1 \end{pmatrix} \frac{\exp(-\frac{1}{2}\Phi_{600}\log R)\tan[(\pi/4)\Phi_{600}]}{1-\chi}\,d\chi$$

$Q_2^{(\mathrm{I})} = 6$
$m\ell pq = -3403 \quad -2802$
$\quad\quad -2412 \quad -1811$
$\quad\quad -1421 \quad\ 0820$
$\quad\quad\ \ 0430$

$$+\text{P.V.} \int_{(a-1)/(a+1)}^{1} \begin{pmatrix} Uf_2 \\ Wh_2 \end{pmatrix} \sum (-1)^{\ell/4} A_{pq}(\chi, \Psi_\ell)/R^q \times \frac{\exp(\frac{1}{2}\Psi_{430}\log R)\cot[(\pi/4)\Psi_{430}]}{1+\chi}\,d\chi$$

$Q_1^{(\mathrm{II})} = 0$ (1st Ref.)
$m\ell pq = 2800$

$$+\text{P.V.} \int_{0}^{1} \begin{pmatrix} -Uf_1 \\ Wh_1 \end{pmatrix} \frac{\exp(-\frac{1}{2}\Phi_{800}\log R)\cot[(\pi/4)\Phi_{800}]}{1-\chi}\,d\chi$$

$Q_1^{(\mathrm{II})} = 0$
$m\ell pq = 1600$

$$-\text{P.V.} \int_{0}^{1} \begin{pmatrix} Uf_1 \\ Wh_1 \end{pmatrix} \frac{\exp(-\frac{1}{2}\Phi_{600}\log R)\tan[(\pi/4)\Phi_{600}]}{1-\chi}\,d\chi$$

$Q_2^{(\mathrm{II})} = 2$
$m\ell pq = -2201$
$\quad\quad -1210$
$\quad\quad -1600$

$$+\text{P.V.} \int_{0}^{1} \begin{pmatrix} Uf_2 \\ Wh_2 \end{pmatrix} [1 - A_{10}(\chi, \Psi_2) - A_{01}(\chi)/R] \times \frac{\exp(\frac{1}{2}\Psi_{210}\log R)\tan[(\pi/4)\Psi_{210}]}{1+\chi}\,d\chi. \tag{33}$$

The functions U, W, f_j and h_j are defined following (17). This sum of integrals appears in the order of their contribution to the response associated with the wave fronts and cusp tips as they are encountered in Fig. 8 from right to left. They are further identified with the wave fronts by the parameters $Q_j^{(\mathrm{I})}$ or $Q_j^{(\mathrm{II})}$ listed on the left of (33), including, in some cases, the number of reflections which have taken place. Also the integers $m\ell pq$ associated with each integral are listed. The value of the phase function giving rise to a wave-front singularity by (25) is indicated by the value or values of m. The integers ℓpq identify the phase functions (23) involved. The third integral for $Q_2^{(\mathrm{I})} = 6$ has a summation which is over all seven combinations of ℓpq listed on the left. Similarly, the sixth integral for $Q_2^{(\mathrm{II})} = 2$ involves three combinations of ℓpq. The fifth integral contains wave-front singularities corresponding to both crossings of $Q_1^{(\mathrm{II})} = 0$.

It should be emphasized that many integrals are not included in (33), which might add small, but nonzero, contributions to the response. However, this is a good approximate response to the impulsive input (2), since the significant values of the response occur near the wave fronts and are contained in the integrals (33). The response to other impulsive inputs (for example, the rectangular impulse $[H(t)-H(t-t_0)]/t_0$ might replace $\delta_+(t)$ in (2))

could be derived by convolution integrals on this representation or on wave-front approximations to (33). The artificial singularities at the wave fronts would be avoided in this manner and the approximation derived from (33) would still be accurate if the inputs were sufficiently sharp.

The integrals in (33) could form the basis of an accurate numerical integration for the high-frequency response. However, (33) will only be approximated by use of (31) and (32). This approximate response is shown at the bottom of Fig. 8 for the displacement component u'. The wave-front singularities are shown directly beneath the corresponding wave fronts.

The approximations near the cusp tips by (32) are minuscule for this particular case, and they are displayed in greatly magnified inserts in Fig. 8. The smallness of these and other contributions for this particular time and location in the plate is attributed to extremely small reflection coefficients.† However, the reflection coefficients are not small everywhere and the results in Fig. 8 serve to illustrate a representative approximate response.

The magnitudes of the singular displacement responses are illustrated in Fig. 8 by vectors attached to the wave fronts. The magnitudes and directions simply result from the approximation (31) and the ratios $\pm Wh_j/Uf_j$, taken from the integrals (33). The three on the right are magnified by amounts indicated on the vectors.

Two interesting reflection coefficients, other than R on (I) and $1/R$ on (II), occur in these representations. The reflection of $Q_1^{(I)} = 0$ (2nd Ref.) into $Q_2^{(I)} = 6$ gives rise to one of these. The rather complicated summation in the third integral in (33) reduces to $R^2(1+R)$ at the wave front $Q_2^{(I)} = 6$. The resulting reflection coefficient is $f_2(1+R)/f_1$ for the displacement component u. The other reflection coefficient is for $Q_1^{(II)} = 0$ into $Q_2^{(II)} = 2$, and it is $f_2(1+1/R)/f_1$ for u.

On (I) R is very small in the approximations for the first three wave responses on the right of Fig. 8, which causes the magnitudes of their singularities to be relatively small. On (II) $1+1/R$ is very small in the approximation near the tip of $Q_2^{(II)} = 2$. The approximation near the tip of $Q_1^{(II)} = 0$ (1st Ref.) is small because f_1 is almost zero.

The displacements on $Q_1^{(II)} = 0$ are essentially in the same direction at both wave fronts, which is contrary to the results in Fig. 7. This is due to the change in sign of f_1 near the tip of $Q_1^{(II)} = 0$ (1st Ref.), just mentioned.

The accuracy of these approximations diminishes rapidly away from the respective wave fronts. It is argued that the response to impulsive inputs is small away from the wave fronts. However, a more exact evaluation of the integrals in (33) and of other contributing integrals would have to be made in order to make definite statements about the response in the gaps between the approximations in Fig. 8.

REFERENCES

[1] P. W. RANDLES and J. MIKLOWITZ, Modal representations for the high-frequency response of elastic plates. *Int. J. Solids Struct.* 7, 1031–1055 (1971).

[2] M. J. P. MUSGRAVE, On whether elastic wave surfaces possess cuspidal edges. *Proc. Camb. phil. Soc. math. phys. Sci.* **53**, 897–906 (1957).

† An error occurs in Ref. [1, p. 1043] for a term used in these calculations. In $E^{(3)}(\chi)$ the term $-\frac{3}{2}(1-\chi)(R^2-1)/(1+\chi)$ should read $-\frac{3}{2}(1-\chi)(R^4-1)/(1+\chi)$.

[3] E. A. KRAUT, Advances in the theory of anisotropic elastic wave propagation. *Rev. Geophys.* **1**, 401–448 (1963).
[4] R. A. SCOTT and J. MIKLOWITZ, Near-field transient waves in anisotropic elastic plates for two and three dimensional problems. *Int. J. Solids Struct.* **5**, 1059–1075 (1969).
[5] A. E. H. LOVE, *A Treatise on the Mathematical Theory of Elasticity*, 4th edition. Dover (1944).
[6] R. A. SCOTT and J. MIKLOWITZ, Transient elastic waves in anisotropic plates. *J. appl. Mech.* **34**, 104–110 (1967).
[7] D. L. ANDERSON, Elastic wave propagation in layered anisotropic media. *J. geophys. Res.* **66**, 2953–2963 (1961).
[8] I. ABUBAKAR, Free vibrations of a transversely isotropic plate. *Q. Jl. Mech. appl. Math.* **15**, 129–136 (1962).
[9] R. K. KAUL and R. D. MINDLIN, Frequency spectrum of a monoclinic crystal plate. *J. acoust. Soc. Am.* **34**, 1902–1910 (1962).
[10] P. W. RANDLES, Modal representations for the high-frequency response of elastic plates, Ph.D. Thesis, California Institute of Technology (1969).
[11] E. A. KRAUT, Propagation of a pulse from a surface line source on a transversely isotropic elastic half-space, Ph.D. Thesis, University of California, Los Angeles (1962).

APPENDIX

Constants appearing in the text are

$$c_j = \frac{c_{33}c_{55}}{c_{55}(c_{11}-c_{55})+(c_{13}+c_{55})^2}+(-1)^j\frac{c_{33}c_{55}}{c_{33}(c_{11}-c_{55})-(c_{13}+c_{55})^2}, \qquad j=1,2,$$

$$c_j = \frac{c_{11}c_{33}}{c_{55}(c_{11}-c_{55})+(c_{13}+c_{55})^2}+(-1)^j\frac{c_{33}c_{55}}{c_{33}(c_{11}-c_{55})-(c_{13}+c_{55})^2}, \qquad j=3,4,$$

$$c_5 = \frac{[c_{55}(c_{11}-c_{55})+(c_{13}+c_{55})^2][c_{33}(c_{11}-c_{55})-(c_{13}+c_{55})^2]}{c_{33}c_{55}(c_{11}-c_{55})^2},$$

$$c_6 = \frac{c_{33}c_{55}(c_{11}-c_{55})/c_{13}}{c_{33}(c_{11}-c_{55})-(c_{13}+c_{55})^2},$$

$$c_j = \frac{c_{13}(c_{13}+c_{55})}{c_{55}(c_{11}-c_{55})+(c_{13}+c_{55})^2}+(-1)^j\frac{c_{13}(c_{13}+c_{55})-c_{33}(c_{11}-c_{55})}{c_{33}(c_{11}-c_{55})-(c_{13}+c_{55})^2}, \qquad j=7,8,$$

$$a = (c_{33}/c_{55})^{\frac{1}{2}}.$$

In the isotropic case, $c_1 = -1$, $c_2 = 3-4\nu$, $c_3 = 0$, $c_4 = 4(1-\nu)$, $c_5 = 1$, $c_6 = (1-\nu)/\nu$, $c_7 = (2-\nu)/(1-\nu)$, $c_8 = -(2-3\nu)/(1-\nu)$ and $a = [2(1-\nu)/(1-2\nu)]^{\frac{1}{2}}$, where ν is Poisson's ratio.

The functions in (28) and (29) are

$$F_1(\chi) = \frac{c_3(g(\chi))^{\frac{1}{2}} + c_4[1+\chi^2 - c_5(1+\chi)^2]}{c_1(g(\chi))^{\frac{1}{2}} + c_2[1+\chi^2 - c_5(1+\chi)^2]}\left[\frac{c_1(1+\chi^2) + c_2(g(\chi))^{\frac{1}{2}}}{c_3(1+\chi^2) + c_4(g(\chi))^{\frac{1}{2}}}\right]^{\frac{1}{2}},$$

$$F_2(\chi) = -\frac{2(g(\chi))^{\frac{1}{2}}[c_1(1+\chi^2) + c_2(g(\chi))^{\frac{1}{2}}]^{\frac{1}{2}}}{(1-\chi)\{c_1(g(\chi))^{\frac{1}{2}} + c_2[1+\chi^2 - c_5(1+\chi)^2]\}},$$

$$F_3(\chi) = \frac{-4c_{33}\chi(1+\chi)/(c_{11} - c_{55})}{\{c_1(g(\chi))^{\frac{1}{2}} + c_2[1+\chi^2 - c_5(1+\chi)^2]\}[c_3(1+\chi^2) + c_4(g(\chi))^{\frac{1}{2}}]^{\frac{1}{2}}},$$

$$F_4(\chi) = \frac{1+\chi}{1-\chi} \cdot \frac{c_1(g(\chi))^{\frac{1}{2}} + c_2[1+\chi^2 - c_5(1-\chi)^2]}{c_1(g(\chi))^{\frac{1}{2}} + c_2[1+\chi^2 - c_5(1+\chi)^2]}.$$

(*Received* 28 *June* 1971; *revised* 1 *March* 1972)

Абстракт—Метод, использованный в предыдущем к изотропным пластинкам, обобщается к анизотропным пластикам, с целью определения переходной характеристики для высокой частоты, для случаев, когда некоторые из фронтов волн являются заострённые. Находится множество фронтов волн, которые происходят в результате многократных отражений в пластинке и которые не существуют для случая изотропии и в некоторых случаях анизотропии. Исходя из интегральных представлений характеристики, определяются приближения фронта волны и приближенная характеристика вблизи концевых частей заострённых фронтов волн.